Acta Geotechnica
https://doi.org/10.1007/s11440-019-00816-8

RESEARCH PAPER

Thermo-mechanical ratcheting in soil–structure interfaces

César Pastén[1] · Emilia Castillo[1] · Song-Hun Chong[2]

Received: 16 May 2018 / Accepted: 14 May 2019

Abstract
This paper proposes and validates a thermo-mechanical ratcheting mechanism that explains the cumulative displacement of soil–continuum interfaces when subjected to temperature cycles and bias forces. The study provides experimental evidence of the mechanism from a physical model consisting of a rectangular, solid prism, that is subjected to temperature cycles and a static bias force aligned parallel to the interface, while resting on a horizontal granular material bed. The experimental results show that the thermally driven displacement accumulates with the number of temperature cycles in the direction of the bias axial force application. In addition, the displacement accumulation rate decreases with the static factor of safety against sliding of the interface and increases with the amplitude of the temperature cycles. FEM thermo-mechanical simulations of the physical model confirm the experimental findings. Finally, the governing equations of the mechanism are captured in a numerical algorithm that solves the load transfer of the prismatic element and reproduces the trend of displacement accumulation.

Keywords Interface · Ratcheting · Thermal cycling · Thermo-mechanical

1 Introduction

Thermo-active geostructures are subjected to temperature changes that may affect the behavior of soil–structure interfaces. In fact, temperature changes and biased forces may cause accumulation of plastic displacement in geosystems consisting of discrete components and interfaces. For instance, thermally driven displacements have been recognized in natural jointed rock slopes [2], where temperature changes accelerate displacement accumulation in the joints due to thermally induced wedging [9, 10]. Unrestrained, exposed geomembranes resting on inclined planes subjected to thermal cycles show displacement accumulation that are inversely proportional to the static factor of safety against sliding and directly proportional to the ratio between the unconstrained thermal elongation and the critical elastic interface displacement [7]. Numerical and experimental analyses of thermo-active piles subjected to thermal cycles, either individual or pile group, show displacement accumulation depending on the static factor of safety and the boundary conditions (i.e., shaft- or end-bearing piles with constant axial load or stiffness) [6, 8, 11].

The mechanical behavior of soil–continuum interfaces at constant ambient temperature has been well documented. The main factors that control the strength and stiffness of these interfaces are the surface roughness and hardness of the continuum material, the grain size distribution and mass density of the soil, and the normal stress applied on the interface, among other factors [4, 5]. For instance, smooth surfaces with low roughness transfer shear load across the interface only by friction, whereas rougher surfaces may mobilize additional passive resistance. On the other hand, laboratory tests performed at different temperatures show that the shear strength of sand–concrete interfaces is not affected by temperature changes unlike clay–concrete interfaces that may change their strength with temperature depending on the degree of over-consolidation [3, 12]. Unfortunately, to the best of the authors' knowledge, no study has been reported on the displacement accumulation in soil–continuum interfaces subjected to cyclic temperature changes.

✉ César Pastén
cpasten@ing.uchile.cl

[1] Department of Civil Engineering, University of Chile, Blanco Encalada 2002, 8370449 Santiago, Chile

[2] Department of Civil Engineering, Sunchon National University, 255, Jungang-ro, Sunchon-si, Jeollanam-do 57922, Republic of Korea

Published online: 28 May 2019

This manuscript develops the thermally induced ratcheting mechanism for a smooth interface, whose failure mode is only due to sliding, demonstrates its occurrence in the laboratory, and analyzes the controlling parameters with the finite element method and a numerical algorithm that solves the governing equations of the phenomenon. Although the conditions investigated in this manuscript do not represent the conditions in real geotechnical applications, this research builds on the current understanding of the thermo-mechanical behavior of soil–structure interfaces.

2 The thermally induced ratcheting mechanism

In order to study the thermo-mechanical ratcheting mechanism, consider a conceptual model that comprises a rectangular, solid prism, length L_T, height H, and width L_W, resting on a horizontal granular material bed (Fig. 1).

The limit axial force F_{max} that can be exerted until the prism slides on the surface is proportional to the prism weight W_T and the friction coefficient of the interface μ

$$F_{max} = W_T \cdot \mu \tag{1}$$

If the exerted axial force F_{axial} is lower than the limit axial force, the interface deforms elastically and the static factor of safety against sliding is:

$$FS = \frac{F_{max}}{F_{axial}} \tag{2}$$

The thermally induced ratcheting mechanism that we propose in this manuscript can be explained as follows: When the rectangular prism expands upon heating, shear stress develops along the prism–soil interface; if the resulting expansion exceeds the critical displacement required to mobilize the interface shear strength, the prism experiences permanent displacement in one of its longitudinal ends and the axial load redistributes; when the prism contracts upon cooling, the equilibrium position is slightly displaced in the direction of the bias axial force. This ratcheting process will continue during the following heating and cooling cycles, accumulating horizontal displacements in the axial direction.

3 Experimental demonstration

3.1 Experimental setup: thermally controlled chamber

A small-scale physical model was built with length L_T = 300 mm, height H = 50 mm, and width L_W = 50 mm. The rectangular prism was manufactured from acrylic in order to provide a high thermal expansion (material properties can be found in Table 1), and the prism's surface in contact with the sand was polished with a fine sand paper to obtain a smooth surface. A uniform sand with a mean particle size d_{50} = 1 mm, specific gravity G_s = 2.65, and coefficient of uniformity Cu = 1.9 was compacted at a density of 1475 kg/m^3 in a wooden box to be used as an underlying material (Fig. 2). The same sand was used in all the tests before leveling the surface in contact with the prism. The prism exerts a normal stress of 579 Pa when resting on the sand.

The model components were housed within a temperature-controlled chamber and instrumented with thermocouples to monitor temperature changes inside the rectangular prism. Heat was provided using a ceramic heat bulb (Fig. 2), and a thermostat modulated the temperature cycles inside the chamber.

The axial force in the rectangular prism was provided with a metallic string attached to a pulley, where a constant load was hung on a basket. Both the pulley and the load were placed outside the temperature-controlled chamber to prevent movements induced by the temperature cycles (Fig. 2). Connecting the basket to a vertical low-friction rail reduced mechanical disturbance from free oscillations. The absolute vertical basket displacements were monitored with a linear variable differential transformer (LVDT). The rectangular prism displacement equals the vertical cart displacement since the thermal expansion of the string is negligible compared to that of the acrylic prism.

The limit axial force required to calculate the factor of safety against sliding was experimentally determined by slowly adding weights to the basket until the rectangular prism slides over the sand surface. The limit axial force was estimated at 2.34 N. Considering that the prism weight is W_T = 8.68 N and combining Eqs. 1 and 2 for the limiting condition (i.e., FS = 1), the friction coefficient of the interface was calculated as μ = 0.27. Note that the weights

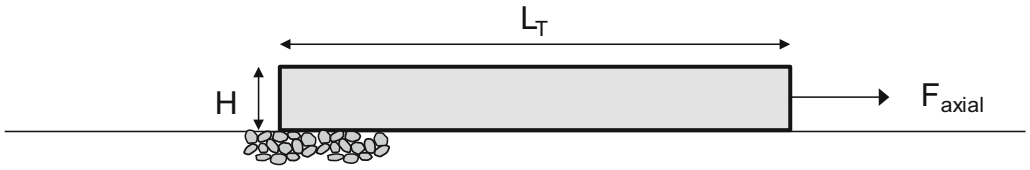

Fig. 1 Conceptual model for thermally induced ratcheting mechanism

Table 1 Thermo-mechanical material properties of the acrylic

Parameter	Symbol	Units	Acrylic
Young's modulus	E	GPa	2.5
Mass density	ρ	kg/m^3	1180
Poisson's ratio	ν	–	0.33
Thermal expansion coefficient	α	10^{-5}/°C	6
Thermal conductivity	k_T	W/m/K	0.19
Specific heat capacity	c_p	J/kg/K	1500
Thermal diffusivity	D_T	m^2/s	1.07×10^{-7}

of the LVDT's core and the basket were also included in the calculation of the limit axial force.

Tests comprise three stages. In the first stage, the model is heated until a constant offset temperature is reached. The second stage consists of cycling the temperature at constant amplitude. Finally, the heat source is turned off allowing the entire system to cool.

3.2 Experimental program

The first part of the experimental program intends to test the influence of the amplitude of the temperature cycles imposed in the second stage of the tests on the displacement accumulation rate. The three tests presented in this section were performed maintaining constant the factor of safety against sliding FS = 2.0. Limitations in our experimental setup made difficult to maintain the period of the temperature cycles constant as the temperature amplitude changes, so both the amplitude and the period of the temperature cycles are changed in the tests. We imposed temperature variations within the chamber that caused cyclic temperature signals inside the rectangular prism (measured as T_{int} in Fig. 2) with the following characteristics: (1) 31 °C DC offset, 1.5 °C peak-to-peak amplitude, and 55-min period (Fig. 3a); (2) 32 °C DC offset, 3.0 °C peak-to-peak amplitude, and 85-min period (Fig. 3b); and (3) 34 °C DC offset, 6.0 °C peak-to-peak amplitude, and 110-min period (Fig. 3c).

The purpose of the second part of the experimental program is to test the influence of the factor of safety against sliding FS for relatively constant amplitudes of the temperature cycles. We imposed three different factors of safety, FS = 12, 2.0, and 1.5, by changing the axial force F_{axial} applied on the rectangular prism in each of the tests. The three performed tests were subjected to temperature variations within the chamber that caused cyclic temperature signals inside the rectangular prism with amplitudes of about 6.0 °C and periods of nearly 3 h. The measured amplitudes and periods of the temperature cycles inside the rectangular prism in each test are shown in Fig. 4a–c, for FS = 12, 2.0, and 1.5, respectively.

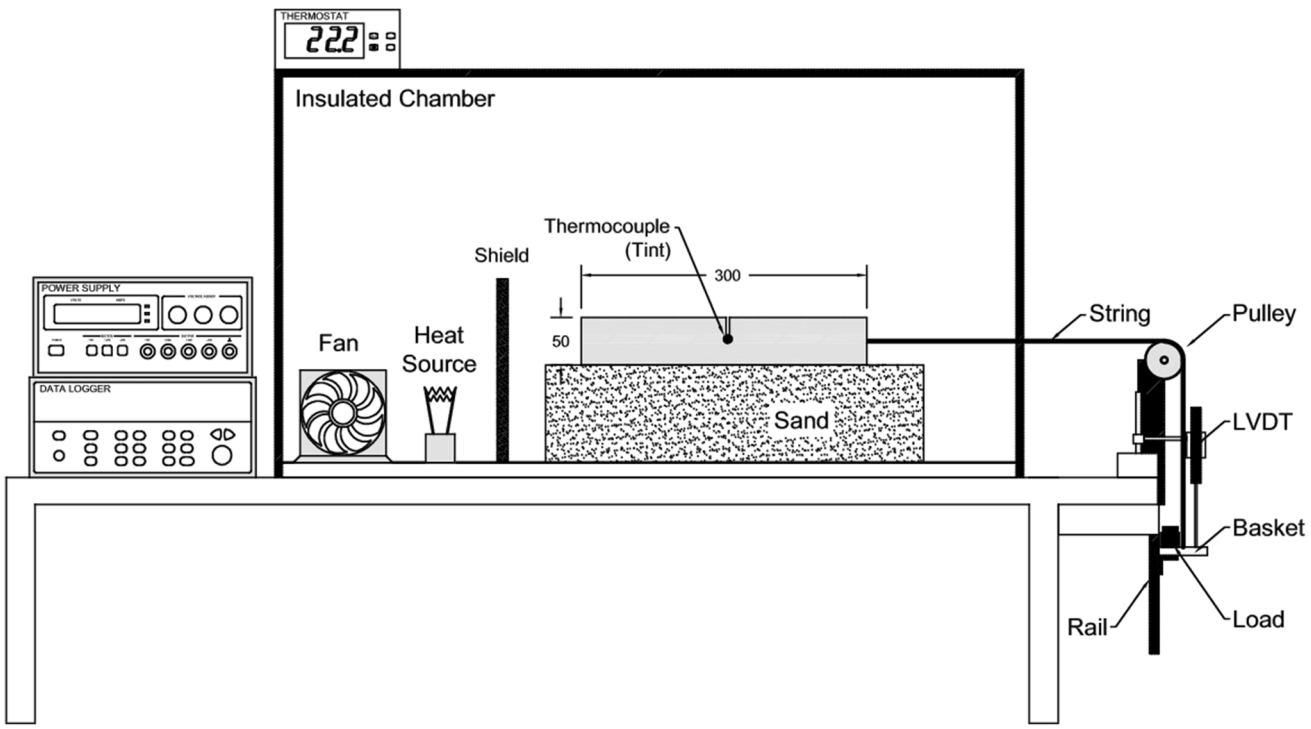

Fig. 2 Experimental setup. Dimensions are in millimeters

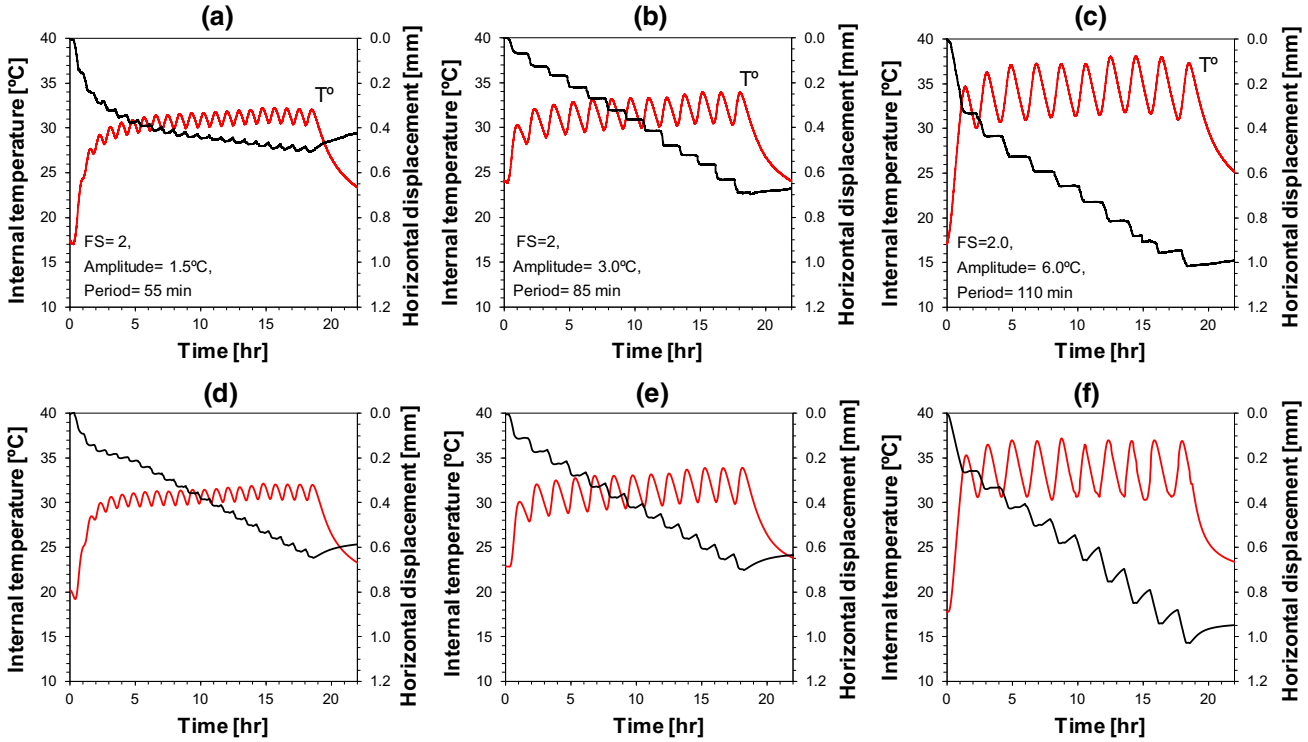

Fig. 3 Comparison of experimental (**a**–**c**) and numerical (**d**–**f**) results regarding period and amplitude of the temperature cycles. The factor of safety against sliding in all cases is FS = 2. Black lines show the prism absolute horizontal displacement, and red lines show the temperature inside the prism (T_{int} in Fig. 2)

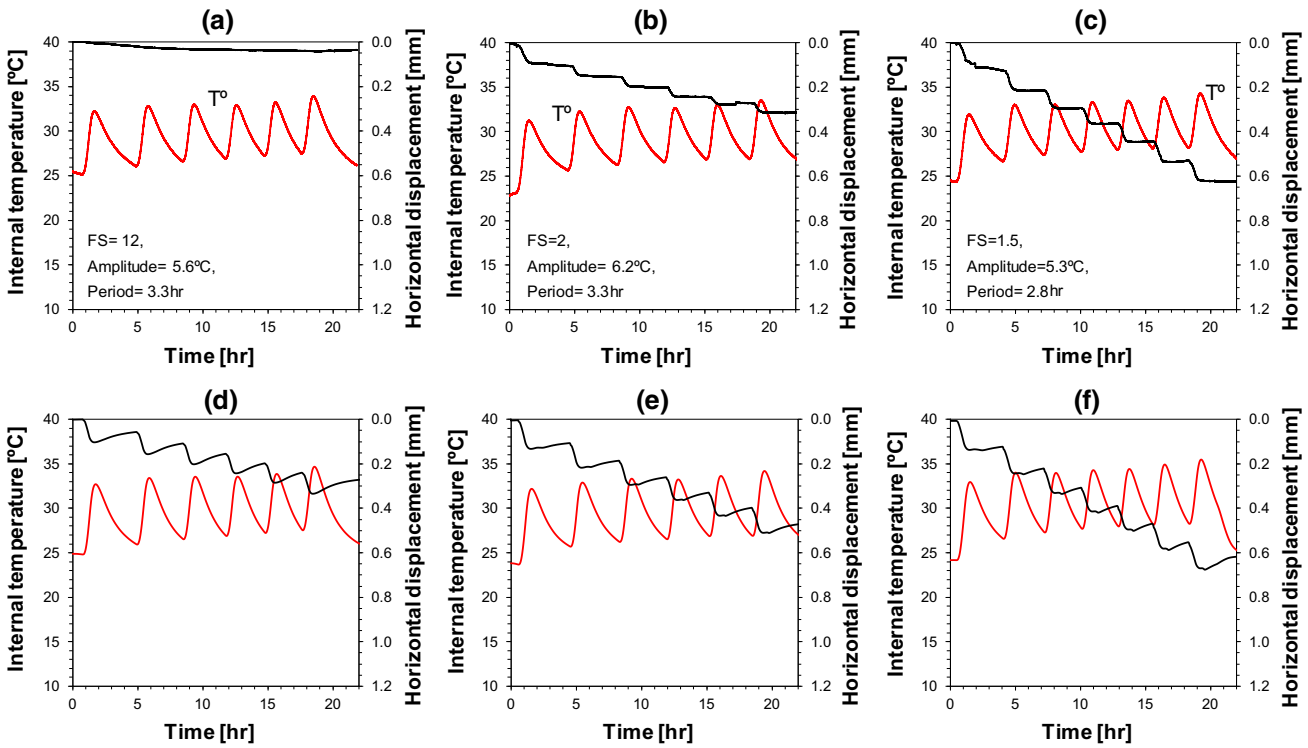

Fig. 4 Comparison of experimental (**a**–**c**) and numerical (**d**–**f**) results regarding the factor of safety against sliding. Black lines show the prism absolute horizontal displacement, and red lines show the temperature inside the prism (T_{int} in Fig. 2)

3.3 Experimental results

Temperature and horizontal prism displacement measurements for different amplitudes of the temperature cycles are shown in Fig. 3. After a fast accumulation of plastic displacement in the first cycles, the accumulation rate decreases with the number of cycles as a result of the first input cyclic temperature signal (Fig. 3a). In contrast, the second and third input cyclic temperature signals result in almost constant displacement accumulation rates of 0.051 mm/cycle (Fig. 3b) and 0.072 mm/cycle (Fig. 3c), respectively. Additional tests not presented in this manuscript suggest that the displacement accumulation increases as the period of the temperature cycles decreases for a constant factor of safety and temperature amplitude. Nonetheless, more tests are required to confirm this behavior.

The effect of the factor of safety against sliding FS for relatively constant amplitudes of the temperature cycles is shown in Fig. 4. The accumulation rates decrease with the factor of safety. A large factor of safety FS = 12 causes almost negligible displacement accumulation rate (Fig. 4a). In addition, the accumulation rate almost doubles when the factor of safety changes from FS = 2.0 to 1.5 (Fig. 4b, c).

4 Numerical simulations

4.1 Numerical model

A numerical model was developed using Abaqus® 6.13 [1]. The material thermo-mechanical properties, the geometry, and the induced cyclic temperature signals were selected to reproduce the experimental conditions.

The interface between the prism and the soil was modeled as a perfect contact interface with an elastic-perfectly plastic shear stress behavior, which is defined by a critical relative displacement to mobilize the interface shear strength δ_c and a friction coefficient μ. In the absence of specific interface data, the critical displacement adopted for all cases that best-fitted the experimental data was $\delta_c = 1 \times 10^{-5}$ m. The friction coefficient of the interface was selected as the value experimentally measured $\mu = 0.27$. The interfaces were assigned a zero thermal conductivity to prevent heat transfer across bodies. All the bodies were modeled as thermo-elastic and discretized with C3D8RT elements (4-nodes, reduced integration, coupled temperature–displacement elements). The soil base and the rectangular acrylic prism properties are listed in Table 1.

Temperature boundary conditions were imposed on all exposed surfaces to emulate the thermal stages observed in the experiments. Boundary conditions were selected to match the measured temperatures inside the prism. Time increments were allowed to vary in order to improve convergence and to ensure that at least 10 temperature increments are applied in every thermal cycle. Following the experimental models, the factors of safety against sliding were set to FS = 12, 2.0, and 1.5 by applying different tensile stresses in the rectangular prism face where the axial force is applied (Fig. 1).

4.2 Numerical results

We performed numerical simulations in order to reproduce the experimental results and compared both outcomes in Figs. 3 and 4. Numerical simulation results for different temperature amplitudes are presented in Fig. 3d–f. In all the three cases, the displacement accumulation rates per cycle are nearly constant. Similar to the experimental results in Fig. 3a, the 1.5 °C peak-to-peak amplitude temperature signal causes the smallest displacement accumulation rate (Fig. 3d), whereas larger accumulated plastic displacements result for temperature signals with peak-to-peak amplitudes of 3.0 and 6.0 °C (Fig. 3e, f, respectively). As in the physical tests, the combination of exposure time and temperature amplitude controls the magnitude of accumulated displacement. Displacement per cycle obtained from the numerical tests (0.049 and 0.085 mm/cycle, Fig. 3e, f) compares reasonably well with values measured in the physical tests (0.051 and 0.072 mm/cycle, Fig. 3b, c) for signals with periods $T = 85$ min and $T = 110$ min and peak-to peak temperature cycle amplitudes $\Delta T = 3$ °C and $\Delta T = 6$ °C, respectively.

Numerical simulation results for factors of safety against sliding FS = 12, 2, and 1.5 are compared to experimental data in Fig. 4d–f. In this case, the displacement accumulation rates are more pronounced than the experimental values. Figure 5 compares the displacement accumulation rates per cycle as a function of the factor of safety obtained from experimental tests and numerical modeling shown in Fig. 4. The figure shows the pronounced increase in the accumulation rate as the factor of safety approaches FS = 1. The numerical simulations over-predict the accumulation rates but follow a similar trend than that of the experimental results.

We believe that the displacement accumulation rate remains constant with the temperature cycles in each of the experimental and numerical tests because no axial boundary condition prevents the accumulation of displacements as long as the contact between the rectangular prism and the underlying soil remains perfectly even. In some experimental tests, interlocking between the sand particles and the edges of the prism may explain the lower displacement accumulation rates.

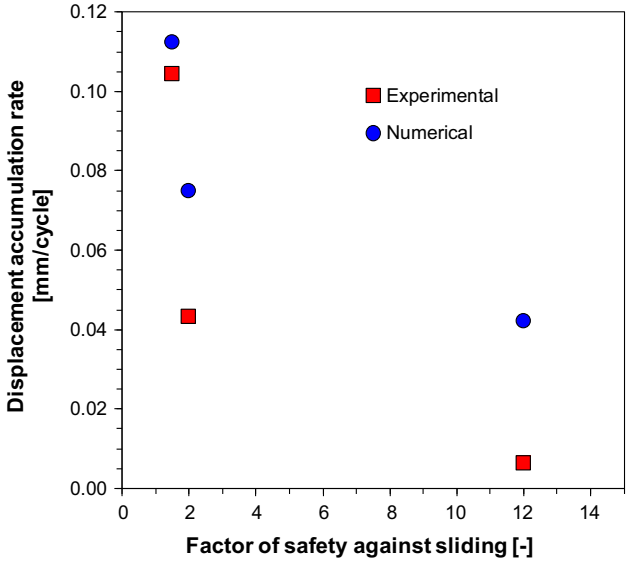

Fig. 5 Comparison of displacement accumulation rates per cycle as a function of the factor of safety against sliding obtained from experimental tests and numerical modeling shown in Fig. 4

5 Numerical algorithm for cyclic thermal loading

5.1 Element-level equilibrium and compatibility

Consider the rectangular prism length L_T (m), height H (m), and the width L_W (m) discretized into N elements of length $L_0 = L_T/N$ (m), so that there are $(N + 1)$ edges. The static axial force applied on the prism is F_{axial} (N). Force equilibrium requires that the axial force on the ith-element left edge F_i (N) equals the sum of the axial force on its right edge F_{i+1} (N) and the shear force at the base interface S_i (N) (Fig. 6a):

$$F_i = F_{i+1} + S_i \tag{3}$$

where the shear force S_i is the mobilized base friction acting on the ith-element s_i (Pa) times the element base contact area:

$$S_i = s_i \cdot L_W \cdot L_0 \tag{4}$$

The base friction s_i (Pa) is assumed to have a linear elastic-perfectly plastic displacement response:

$$s_i = s_i(\delta_i, \delta_{i+1}) = \begin{cases} -s_i^{ult} & \text{if} \quad \left(\frac{\delta_i + \delta_{i+1}}{2}\right) \le -\delta_c \\ k_i\left(\frac{\delta_i + \delta_{i+1}}{2}\right) & \text{if} \quad -\delta_c < \left(\frac{\delta_i + \delta_{i+1}}{2}\right) < \delta_c \\ s_i^{ult} & \text{if} \quad \delta_c \le \left(\frac{\delta_i + \delta_{i+1}}{2}\right) \end{cases} \tag{5}$$

where δ_i (m) and δ_{i+1} (m) are the relative prism–soil displacements at the element left and right edges, $k_i = s_i^{ult}/\delta_c$ (Pa/m) is the interface stiffness, and δ_c (m) is the critical relative displacement to mobilize the prism–soil shear strength s_i^{ult} (Pa). The prism–soil shear strength at the ith-element $s_i^{ult} = \sigma_{vi} \cdot \mu$ combines the vertical stress $\sigma_{vi} = H \cdot \rho \cdot g$ (Pa) and the prism–soil interface friction coefficient μ (–).

Consider a uniform prism temperature increase. Thermal expansion of the ith-element is constrained by the change in axial forces acting on the element. Displacement compatibility requires that the change in the element length $\Delta_i = \delta_{i+1} - \delta_i$ (m) equals the free thermal elongation Δ_i^T (m) minus the elastic mechanical contraction $\Delta\sigma_i$ (m):

$$\Delta_i = \delta_{i+1} - \delta_i = \Delta_i^T - \Delta_i^\sigma \tag{6}$$

The free thermal elongation $\Delta_i^T = \alpha \cdot \Delta T \cdot L_0$ is computed from the thermal expansion coefficient α (°C^{-1}) and the amplitude of the temperature change ΔT (°C). On the other hand, the elastic mechanical contraction is:

$$\Delta_i^\sigma = \frac{F_i + F_{i+1}}{2}\frac{L_0}{AE} \tag{7}$$

where $A = H \cdot L_w$ (m^2) is the prism's transverse area and E (Pa) is the prism's Young's modulus.

Combining equilibrium and compatibility conditions (Eqs. 3, 6), the displacement of the ith-element left edge δ_i is obtained as a function of the ith-element right-edge displacement δ_{i+1} and axial force F_{i+1}:

$$\delta_i(\delta_{i+1}, F_{i+1}) = \begin{cases} \delta_{i+1} + \frac{L_0}{2AE}\left(2F_{i+1} - L_W L_0 s_i^{ult}\right) - \Delta_i^T \\ \quad \text{if} \quad \left(\frac{\delta_i + \delta_{i+1}}{2}\right) \le -\delta_c \\ \dfrac{\delta_{i+1}\left(1 + \frac{L_0^2 L_W k_i}{4AE}\right) + \frac{L_0}{AE}F_{i+1} - \Delta_i^T}{1 - \frac{L_0^2 L_W k_i}{4AE}} \\ \quad \text{if} \quad -\delta_c < \left(\frac{\delta_i + \delta_{i+1}}{2}\right) < \delta_c \\ \delta_{i+1} + \frac{L_0}{2AE}\left(2F_{i+1} + L_W L_0 s_i^{ult}\right) - \Delta_i^T \\ \quad \text{if} \quad \delta_c \le \left(\frac{\delta_i + \delta_{i+1}}{2}\right) \end{cases} \tag{8}$$

5.2 Numerical algorithm

Equations 3 through 8 allow tracking of the evolution of the prism axial force and displacement during thermal cycles. The equilibrium condition for the prism when subjected to a constant temperature change ΔT is calculated from the most right edge of the prism $i = (N + 1)$, where

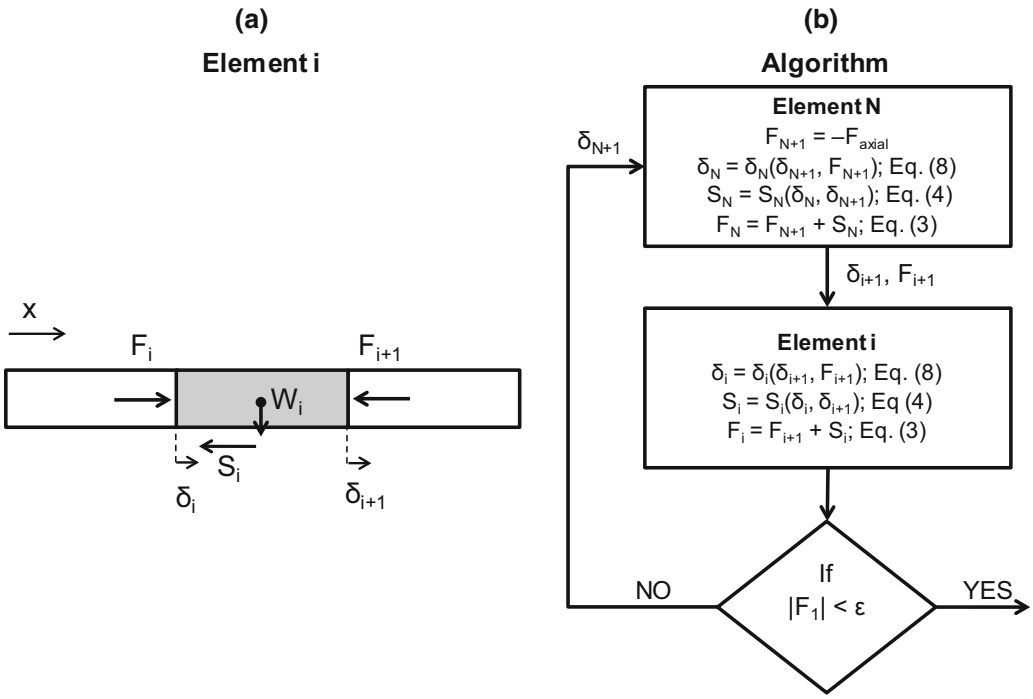

Fig. 6 Numerical algorithm for a prism subjected to temperature cycles. **a** Forces and relative displacements of the *i*th-element. **b** Solution of the numerical algorithm

the axial force is applied, to the first edge of the prism $i = 1$. The iterative algorithm follows:

1. Impose a relative displacement at the *N*th-element right edge δ_{N+1} and compute the relative displacement at the *N*th-element left edge δ_N, considering $F_{N+1} = -F_{\text{axial}}$ (Eq. 8).
2. Calculate the *N*th-element shear force S_N (Eqs. 4, 5) and axial force on its left edge F_N (Eq. 3).
3. Use the relative displacement δ_N and the axial force F_N to equilibrate the element $i = (N - 1)$. Then, continue element-by-element to reach the first element $i = 1$.
4. Verify the computed value of the axial force on the first element left edge F_1. If $|F_1| > \varepsilon$, where ε (N) is a preselected tolerance value, the iterative procedure is repeated for a different relative displacement value δ_{N+1} in step 1. If $|F_1| \leq \varepsilon$, the solution has converged.

5.3 Load–transfer curves

The load–transfer curves for the static load without heating are obtained using $\Delta_i^T = 0$ in Eq. 6. The application of thermal cycles is imposed once the axial load at the prism boundary is equilibrated. Thermal cycles consist of a sequence of positive and negative temperature changes using the algorithm described above. The cyclic temperature change amplitude ΔT is assumed constant along the prism. As implemented, the algorithm does not account for thermo-mechanical effects in the soil.

The numerical algorithm was used to study the load–transfer curves of the prism subjected to cyclic temperature changes with peak-to-peak amplitude of 6 °C (similar to the conditions in Fig. 3c). The model parameters adopted in this simulation are shown in Table 1. For a factor of safety FS = 2.0, the axial load is $F_{\text{axial}} = 1.17$ N and the maximum mobilized shear force at the base is $S_{\text{max}} = 0.047$ N when the prism is discretized into $N = 50$ elements (Fig. 7a). Under the application of the static axial load, the distribution of axial force is linear from the free end ($x/L = 0$) to the end where the axial load is applied ($x/L = 1$), whereas both the friction resistance and the normalized interface displacement are constant along the prism.

The numerical results shown in Fig. 7a indicate that the friction resistance is completely mobilized at both ends of the prism upon heating. As a result, the left half of the prism displaces to the left and the right half displaces to the right. When the prism cools, a constant relative displacement remains. Thermal expansion and contraction of the prim cause a reversal of relative displacements with respect to the "neutral point" and a linear accumulation of displacements with the number of thermal cycles (0.007 mm/cycle). The load–transfer curves do not change with the successive temperature cycles.

If the axial load increases to $F_{\text{axial}} = 1.56$ N, the factor of safety reduces to FS = 1.5 and the maximum shear force mobilized at the base remains $S_{\text{max}} = 0.047$ N (Fig. 7b). In this case, the larger extend of the mobilized base frictional

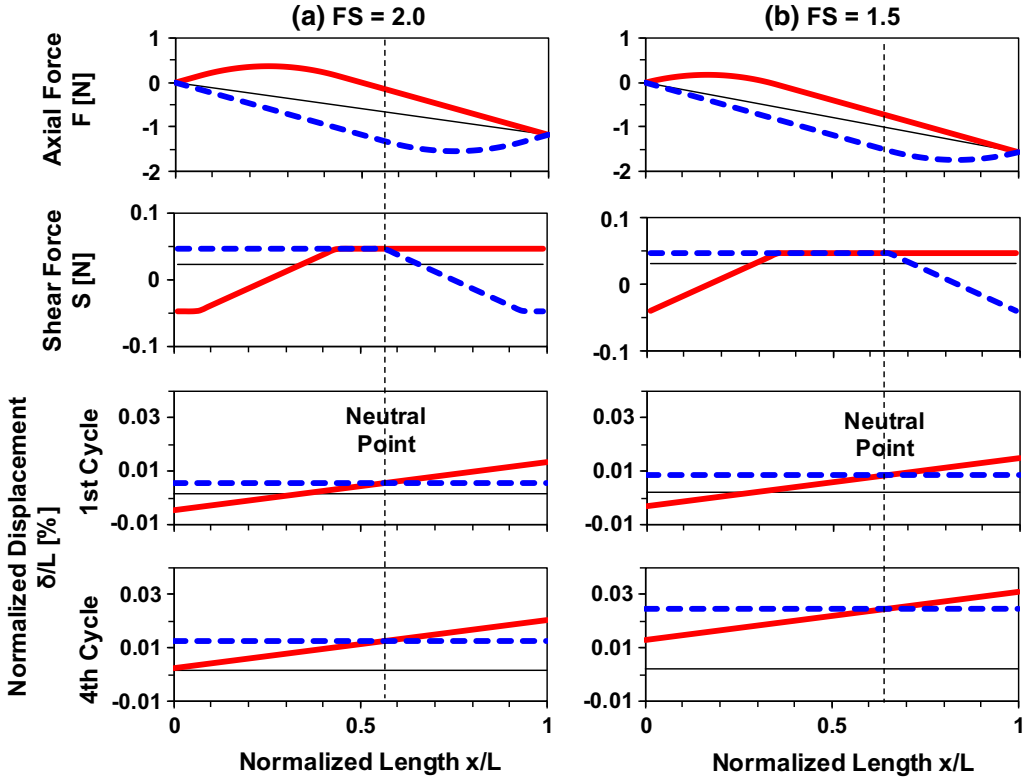

Fig. 7 Load–transfer curves for cyclic temperature changes obtained with the numerical algorithm. The factors of safety against sliding are **a** FS = 2.0 and **b** FS = 1.5. Continuous curves correspond to a heating phase and dotted lines to a cooling phase. The prism was discretized into 50 elements, and the parameters used in the simulation are listed in Table 1

resistance displaces the "neutral point" toward the end where the axial load is applied and accelerates the ratcheting displacement of the prism (0.016 mm/cycle). This mechanism explains the experimental results shown in Fig. 4.

6 Conclusions

The proposed conceptual model captures the thermally induced ratcheting mechanism relevant to geosystems composed of elements and interfaces subjected to bias forces and temperature cycles. Experimental and numerical results show that thermo-mechanical coupling can lead to displacement accumulation and ratcheting in the interface.

Experimental results from the physical modeling show that the displacement accumulates in the direction of the bias force application and that the displacement accumulation rate is proportional to the amplitude of the temperature cycles. In addition, the accumulation rate decreases with the static factor of safety against sliding of the interface. Interfaces at the verge of static instability (FS $\approx$ 1) are expected to be more susceptible to thermally induced ratcheting.

A simplified 3D FEM numerical model composed of an elastic rectangular prism and an elastic-perfectly plastic interface is able to capture the mechanism. Numerical results showed that the displacement accumulation rates are consistent with experimental results from physical models.

Finally, the governing equations are captured in a numerical algorithm that considers the thermo-mechanical interaction of the prism and the base interface. The obtained 1D load–transfer curves show the distribution of axial and shear force that explains the accumulation of displacements as a function of the factor of safety. The analytical model anticipates that the rate of displacement accumulation increases with the prism length and decreases with the critical relative displacement to mobilize the prism–soil shear strength.

The experimental and numerical results reported in this paper intend to demonstrate the thermally induced ratcheting mechanism rather than reproducing conditions expected in real geotechnical applications. We acknowledge that the surface roughness, grain size distribution, and normal effective stresses, among other factors, may hinder or enhance this thermo-mechanical mechanism in real applications.

Acknowledgements Support for this research was provided by the CONICYT FONDECYT Initiation into Research Grant No. 11130363. Part of the experimental setup was constructed by F. Muñoz. C. Pastén thanks Dr. J.C. Santamarina for generously sharing the research idea.

References

1. Abaqus (2013) ABAQUS version 6.13. Dassault Systémes SIMULIA Corporation, Providence
2. Bakun-Mazor D, Hatzor YH, Glaser SD, Santamarina JC (2013) Thermally vs. seismically induced block displacements in Masada rock slopes. Int J Rock Mech Min Sci 61:196–211
3. Di Donna A, Ferrari A, Laloui L (2016) Experimental investigations of the soil–concrete interface: physical mechanisms, cyclic mobilization, and behaviour at different temperatures. Can Geotech J 53(4):659–672
4. Frost JD, DeJong JT, Recalde M (2002) Shear failure behavior of granular-continuum interfaces. Eng Fract Mech 69(17): 2029–2048
5. Martinez A, Frost JD (2017) The influence of surface roughness form on the strength of sand–structure interfaces. Géotech Lett 7(1):104–111
6. Nguyen VT, Tang AM, Pereira JM (2017) Long-term thermo-mechanical behavior of energy pile in dry sand. Acta Geotech 12(4):729–737
7. Pastén C, Santamarina JC (2014) Experimental and numerical modeling of thermally-induced ratcheting displacement of geomembranes on slopes. Geosynth Int 21(6):334–341
8. Pastén C, Santamarina JC (2014) Thermally induced long-term displacement of thermoactive piles. J Geotech Geoenviron Eng 140(5):06014003
9. Pastén C, García M, Cortés DD (2015) Physical and numerical modelling of the thermally induced wedging mechanism. Géotech Lett 5(3):186–190. https://doi.org/10.1680/jgele.15.00072
10. Pastén C, García M, Santamarina JC (2015) Thermo-mechanical ratcheting in jointed rock masses. Geotech Lett 5(2):86–90. https://doi.org/10.1680/geolett.14.00118
11. Suryatriyastuti ME, Burlon S, Mroueh H (2016) On the understanding of cyclic interaction mechanisms in an energy pile group. Int J Numer Anal Methods Geomech 40(1):3–24
12. Yavari N, Tang AM, Pereira JM, Hassen G (2016) Effect of temperature on the shear strength of soils and the soil–structure interface. Can Geotech J 53(7):1186–1194